analytical chemistry

pubs.acs.org/ac Article

# Correlative Imaging of Trace Elements and Intact Molecular Species in a Single-Tissue Sample at the 50 μm Scale

Janella Marie de Jesus, Catia Costa, Amy Burton, Vladimir Palitsin, Roger Webb, Adam Taylor, Chelsea Nikula, Alex Dexter, Firat Kaya, Mark Chambers, Veronique Dartois, Richard J. A. Goodwin, Josephine Bunch, and Melanie J. Bailey*

Cite This: *Anal. Chem.* 2021, 93, 13450−13458 Read Online

ACCESS | Metrics & More | Article Recommendations | Supporting Information

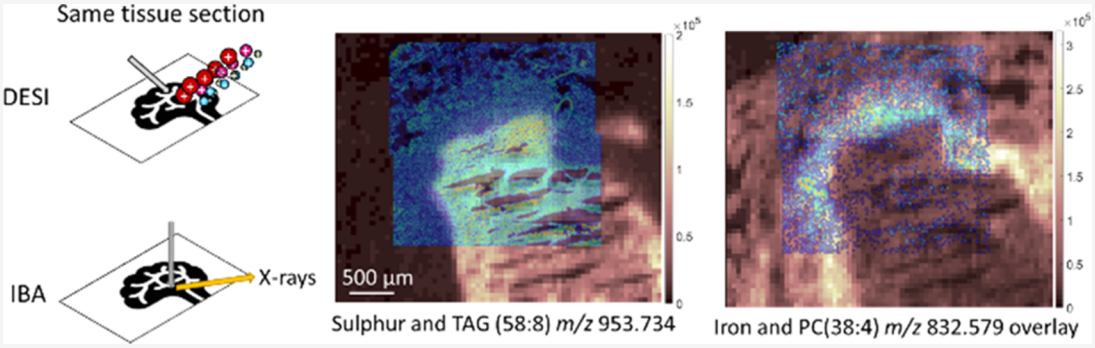


**ABSTRACT:** Elemental and molecular imaging play a crucial role in understanding disease pathogenesis. To accurately correlate elemental and molecular markers, it is desirable to perform sequential elemental and molecular imaging on a single-tissue section. However, very little is known about the impact of performing these measurements in sequence. In this work, we highlight some of the challenges and successes associated with performing elemental mapping in sequence with mass spectrometry imaging. Specifically, the feasibility of molecular mapping using the mass spectrometry imaging (MSI) techniques matrix-assisted laser desorption ionization (MALDI) and desorption electrospray ionization (DESI) in sequence with the elemental mapping technique particle-induced X-ray emission (PIXE) is explored. Challenges for integration include substrate compatibility, as well as delocalization and spectral changes. We demonstrate that while sequential imaging comes with some compromises, sequential DESI-PIXE imaging is sufficient to correlate sulfur, iron, and lipid markers in a single tissue section at the 50 μm scale.

## INTRODUCTION

Studying the spatial distribution of molecular and elemental signals has wide-ranging applications from healthcare to forensics and environmental sciences. In biomedical science, elemental and molecular markers play a key role in the study of disease characterization and progression.[1] Colocation of molecular markers within discrete features in tissues may result in better development of new therapeutics, preventative care, and optimal treatment.[2−5]

Elemental mapping has been widely used to explore the distribution of elements in tissue for disease pathogenesis[6−10] and to determine elemental differences between "healthy" and "non-healthy" cells.[2,5,11−14] A limited number of recent publications have dealt with multimodal imaging to colocate elemental and molecular markers.[15−20] For example, Matusch et al. reported the use of laser ablation inductively coupled plasma mass spectrometry (LA-ICP-MS) and matrix-assisted laser desorption ionization (MALDI) to colocate elemental and molecular markers in adjacent mouse brain samples at the 150 μm scale. Touboul *et al.* reported elemental imaging using secondary ion mass spectrometry (SIMS) with 3.9 μm resolution and molecular imaging using MALDI at 150 μm.[20] More recently, Flint et al. applied desorption electrospray ionization (DESI), LA-ICP-MS, and imaging mass cytometry (IMC) to three-dimensional (3D) cell culture (termed an "aggregoid"), to provide images of tricarboxylic acid (TCA) cycle metabolites, endogenous elements (LA-ICP-MS), and elemental tags attached to proteins.[21] However, none of these studies used the same tissue sample, presumably due to incompatible sample handling requirements and a lack of information about the impact of performing sequential measurements on the same tissue. As imaging techniques move toward the micron scale, analysis of sequential tissue

Received: May 6, 2021
Accepted: July 30, 2021
Published: October 1, 2021

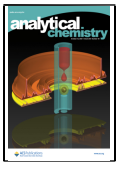







https://doi.org/10.1021/acs.analchem.1c01927
*Anal. Chem.* 2021, 93, 13450−13458

sections is undesirable. This is because features at this scale may not be accurately reproduced in sequential sections.

Elemental and molecular imaging of the same tissue section has only been performed sparingly. Svirkova et al. reported imaging of the same undecalcified tissue sections by micro X-ray fluorescence ($\mu$-XRF) and MALDI.[19] Here, it was found that significant compromises had to be made to successfully achieve sequential imaging. To achieve images of the minor elements S, Ca, and P, it was necessary to use Kapton tape to support the tissue, but this was found to affect the laser beam behavior, restricting the MALDI spatial resolution to 150 $\mu$m.

It should also be noted that simultaneous molecular and elemental imaging of tissues and cells is possible at submicron dimensions using SIMS.[22] However, drawbacks of SIMS imaging are the high levels of fragmentation of intact biomolecules and the difficulty in obtaining a quantitative analysis of elemental (and molecular) species due to matrix effects.

Ion beam analysis (IBA) techniques such as particle-induced X-ray emission (PIXE) and elastic backscattering spectrometry (EBS) are quantitative and have been useful in biomedical investigations since the 1980s for providing high spatial resolution (<1 $\mu$m) images of trace elements.[23−30] IBA techniques use an MeV energy ion beam (normally protons or $\alpha$ particles), to generate X-rays, $\gamma$ rays, and scattered particles, which are measured simultaneously to provide full mass closure of trace, major, and minor elements in a sample.[27]

In PIXE, the ion beam causes the ejection of an electron from the inner shell of an atom, creating a "hole," which is immediately filled by an electron from an outer shell. This results in the emission of X-rays characteristic of the target element.[31,32] In EBS, on the other hand, the incident MeV ion scatters from the target nuclei, with an energy that is dependent primarily on the mass of the target atom and the depth at which the collision took place. It is therefore possible to determine depth profiles of major elements in a sample. The collection of EBS with PIXE spectra allows for a 3D representation of the elemental composition of a sample from a single measurement.

IBA techniques offer parts per million sensitivity and submicron spatial resolution.[14,33] Uniquely, the backscattered particle spectra generated by IBA techniques can simultaneously provide information on elemental depth distributions, light elements (C, N, O), and sample thickness. This information can be used to account for X-ray absorption and therefore correct for matrix effects in the X-ray images. In contrast, one of the limitations of LA-ICP-MS, XRF, and SIMS is that matrix-matched samples are required for quantification,[34] which is not the case for IBA techniques.

More recently, efforts have been directed toward exploiting the target molecules and fragments that are ejected during ion bombardment—so-called MeV secondary ion mass spectrometry (MeV-SIMS).[35−38] This method holds significant promise for mass spectrometry at submicron resolution but is not routinely available. In contrast, the mass spectrometry imaging (MSI) techniques MALDI and DESI have become widely adopted and are steadily improving in their spatial resolution, with spot sizes of 12 $\mu$m (DESI)[39] and 1.4 $\mu$m (MALDI)[40] having been previously reported. Indeed, these image resolutions are now approaching dimensions suitable for their meaningful integration with IBA. We therefore evaluate the possibility of carrying out DESI and MALDI imaging in sequence with IBA, for the colocalization of molecular and elemental markers.

Biological tissues are inherently heterogeneous, making it difficult to assess any artifacts caused by sequential imaging. In this work, homogenized tissue was used as a spatially uniform "standard tissue." This allowed a range of different substrates to be tested for compatibility with both molecular and elemental imaging. The optimal sequence of analysis, i.e., IBA followed by MSI or MSI followed by IBA was then explored. Finally, a practical application of DESI-IBA imaging to colocate elemental and molecular markers of tuberculosis in rabbit lung tissue is demonstrated. The work presented will be of significant interest to researchers developing integrated imaging for greater characterization of diseases and those exploring new treatments.

## MATERIALS AND METHODS

**Sample Preparation.** *Homogenized Tissue.* Liver homogenates were prepared as described by Swales et al.[41] Liver tissue was homogenized and pipetted into molds (2 mL Pasteur pipette bulb) and then frozen at −80 °C. Samples were sectioned to 10 $\mu$m thick using a Thermo NX70 Cryostar (ThermoScientific, Germany) and thaw-mounted onto various substrates before being vacuum packed and stored at −80 °C. Samples were brought to room temperature in the vacuum packing prior to analysis. All animals and tissues were managed in accordance with the U.K. Home Office Animals (Scientific Procedures) Act 1986. The organs used within this study are additionally used within the 3Rs principles as they comprise control material surplus to the original study for which they were intended.

*Fresh Frozen Lung Tissue.* Rabbit infection and sample collection were performed in Biosafety Level 3 (BSL3) facilities and approved by the Institutional Animal Care and Use Committee of the National Institute of Allergy and Infection Disease, NIH, Bethesda, MD (Protocol number LCIM-3). All studies followed the guidelines and basic principles stated in the United States Public Health Service Policy on Humane Care and Use of Laboratory Animals. All samples collected from *Mycobacterium tuberculosis*-infected animals were handled and processed in the BSL3 in compliance with protocols approved by the Institutional Biosafety Committee of the National Institute of Allergy and Infection Disease, NIH, and Hackensack Meridian Health, NJ.

Female New Zealand White (NZW) rabbits weighing 2.2−2.6 kg were maintained under specific pathogen-free conditions and fed water and chow ad libitum. NZW rabbit ID 713 was infected with *M. tuberculosis* HN878, using a nose-only aerosol exposure system as described.[42] At 12 weeks post infection, once mature cellular and necrotic lung lesions had developed,[43] the rabbit received 28 daily doses of bedaquiline at 20 mg/kg. Twenty-four hours after the last dose, lung lesions embedded in the surrounding tissue were collected for imaging and snap-frozen in liquid nitrogen vapor as described previously.[44] To sterilize the samples and inactivate all viable *M. tuberculosis* bacilli, samples were $\gamma$-irradiated in a Co-60 irradiator until exposure reached 3 Mrad (validated as a sufficient exposure to kill all viable *M. tuberculosis* bacteria present in lung lesions). Dry ice was resupplied as required to keep the samples frozen at all times. The frozen rabbit lesions were sectioned at 10 $\mu$m thickness using a CM1860 UV cryostat (Leica) at −20 °C. The sections were thaw-mounted onto 1.4 $\mu$m thick poly(ethylene terephthalate) (PET)


https://doi.org/10.1021/acs.analchem.1c01927
Anal. Chem. 2021, 93, 13450−13458

membrane slides (Leica), shipped on dry ice, and stored at −80 °C.

*Support Substrates.* Candidate substrates were poly(ethylene terephthalate) (PET) films (Leica, U.K.), carbon foil, and highly ordered pyrolytic graphite (HOPG) (both from Goodfellow, UK), silicon wafers, and Superfrost glass slides (ThermoScientific, U.K.). The carbon foil and HOPG were both washed with acetone and isopropanol prior to mounting the tissue sample. For further details, see Supporting Information Table S1.

*IBA.* Ion beam analysis (IBA) was carried out at the University of Surrey Ion Beam Centre. Samples were analyzed using 2.5 MeV protons, with beam currents ranging from 300 to 600 pA. The beam was focussed to ∼2 μm × 2 μm (measured using a 1000 copper grid). The scan size was 2 mm × 2 mm, with the beam scanned in a raster pattern. The exception was the rabbit lung tissue sections, where the 2 mm × 2 mm areas were divided into four 1 mm × 1 mm squares.

X-rays were detected using a Si(Li) detector (for analysis of the tissue homogenates) or silicon drifted detector (SDD; for the rabbit lung tissue) with a 130 μm beryllium (Be) foil to stop backscattered particles reaching the detector. This also attenuated X-rays coming from elements with Z < Al. For analysis of tissue on the silicon substrate, a 50 μm kapton filter was used to preferentially attenuate Si K X-rays. Backscattered particles were detected using a PIPS charged particle detector (Mirion Technologies) with an active area of 150 $mm^2$. The X-ray and backscattered particle detector responses were calibrated using a BCR-126A glass standard[45] (European Commission, Joint Research Centre (JRC), Geel, Belgium). Data were acquired and analyzed using OMDAQ-3 software (Oxford Microbeams, Ltd. UK).

To understand the impact of prior PIXE analysis on molecular species, separate areas of tissue homogenates were analyzed by PIXE at three different fluences: $2.5 \times 10^{13}$ ions/$cm^2$, $3.0 \times 10^{14}$ ions/$cm^2$, and $6.0 \times 10^{14}$ ions/$cm^2$. This corresponded to acquisition times of 5 min, 1 and 2 h.

*DESI.* For imaging of tissue homogenates, a DESI source (Waters, MA) was coupled to a Synapt G2-Si High Definition Q-ToF (Waters, U.K.) mass spectrometer. A 95:5 (% v/v) methanol/water spray solvent was delivered at a rate of 2 μL/min using a Mitos P-pump (Dolomite Microfluidics, U.K.), with an electrospray voltage of 4 kV. Calibration of spectra was carried out using a polylactic acid (PLA) sublimed slide (made in-house) with a collision energy setting of 35 V and capillary temperature set to 100 °C. Data were acquired in positive ion "resolution" mode, at a mass range of $m/z$ 100−1200 and a calculated mass resolving power of 15 000 at $m/z$ 200. The imaging region was selected using HDI Imaging (Waters, U.K.). The nominal pixel size was 75 μm using a stage speed of 150 μm/s and a scan time of 0.485 s.

For the imaging of TB rabbit lesions, DESI was carried out using a Waters (Waters, MA) prototype source, coupled to a XeVo G2 XS ToF (Waters, U.K.). Spray solvent of 95:5 methanol/water was sprayed at a flow rate of 2 μL/min using an Ultimate 3000 Pump (ThermoScientific, Germany). Data was acquired with a 0.6 kV capillary voltage, at a mass range of $m/z$ 100−1200. The nominal pixel size 50 μm with the stage speed set at a rate of 100 μm/s and a scan time of 0.486 s.

*MALDI.* Prior to analysis, tissue homogenates were brought to room temperature in a vacuum desiccator for 20 min. The sample was then sprayed with α-cyano-4-hydroxycinnamic acid CHCA matrix (Sigma-Aldrich, U.K.) prepared in 80:20 methanol/water (% v/v) to a concentration of 5 mg/mL. The matrix was deposited using a pneumatic sprayer (TM Sprayer, HTX Imaging), using a heated spray head at 65 °C, flow rate of 0.07 mL/min, and pressure of 15 mBar. The spray head was moved across the sample at 1333 mm/min in a sawtooth pattern for 16 passes, giving a calculated matrix thickness of 1 μm.

MALDI imaging was performed on a Synapt G2-Si High Definition Q-ToF mass spectrometer (Waters). Data was acquired in positive ion resolution mode across a mass range of $m/z$ 100−1200 at a calculated resolving power of 15 000 at $m/z$ 200. A Nd:YAG laser (355 nm) was used with a repetition rate of 2000 Hz, a calculated laser energy of 3.6 μJ, and a laser spot size of 157 μm × 222 μm. The scan time was set to 0.1 s and the nominal pixel size was 45 μm.

*Data Analysis—MSI.* Waters RAW data were converted into the appropriate imzML format through a two-step conversion, first by conversion to mzML using Proteowizard,[46] then to an imzML converter.[47] The imzML data was analyzed using Spectral Analysis[48] (version 1.4.0), which was run using Matlab (version 2017b). Prior to generating a mean spectrum, data were preprocessed using a rebinning method (bin size of 0.001) and normalized to the total ion intensity.

## RESULTS

**Substrate Compatibility.** To correlate features at the micron scale, it is necessary to study thin sections of tissue. This means mounting the tissue on a flat substrate, which acts as a mechanical support. Glass slides are typically used for MSI, due to the compatibility with traditional staining methods. However, glass is not a suitable support for PIXE (or indeed any X-ray spectrometry method) imaging due to the presence of impurities.[49] Instead, the substrate should contain low elemental impurities, should not charge upon irradiation, and should be of a low Z. This is to reduce secondary Bremsstrahlung radiation and other background interferences in the X-ray spectra.

Previous PIXE imaging experiments have used tissue samples suspended over an open hole, but this is not suitable for thin sections. Other approaches include Kapton, pioloform, polypropylene, or mylar stretched over a metal frame, which are typically produced in-house.[50−52] Our initial experiments showed that in-house generated foils lacked the rigidity needed to provide clear mass spectrometry images (Supporting Information Figure S2).

Therefore, candidate substrates were chosen with low Z and high mechanical rigidity. These were silicon wafer, polyethylene (PET) films, carbon foil, and highly ordered pyrolytic graphite (HOPG). To benchmark the quality of mass spectrometry images produced on these new substrates for mass spectrometry imaging, tissues were also mounted on glass slides. Importantly, thin sections of homogenized tissue were used as a spatially uniform sample to allow meaningful comparison of images and spectra.

*IBA.* Supporting Information Figure S3 shows example PIXE spectra for each substrate chosen for compatibility testing. PIXE measurements were taken from the substrate with and without a tissue homogenate, to determine elemental impurities in the substrate and the sensitivity to trace elements in the tissue. In the PET substrate, only Ca was detected at >3× LoD. For carbon foil, HOPG, and Si, at least two elemental impurities were detected at this level (Supporting Information Table S2).


https://doi.org/10.1021/acs.analchem.1c01927
Anal. Chem. 2021, 93, 13450−13458

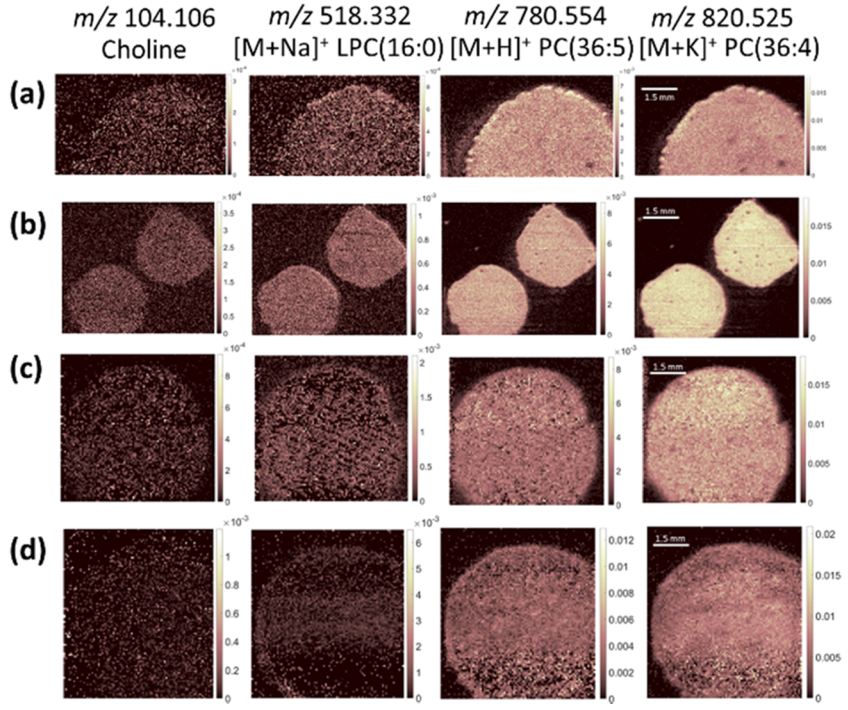


**Figure 1.** Extracted ion images for choline, $[M + Na]^+$ LPC(16:0), $[M + H]^+$ PC(36:5), and $[M + K]^+$ PC(36:4) from DESI-MSI acquisition on tissue homogenates mounted on (a) glass, (b) PET, (c) HOPG, and (d) carbon foil.

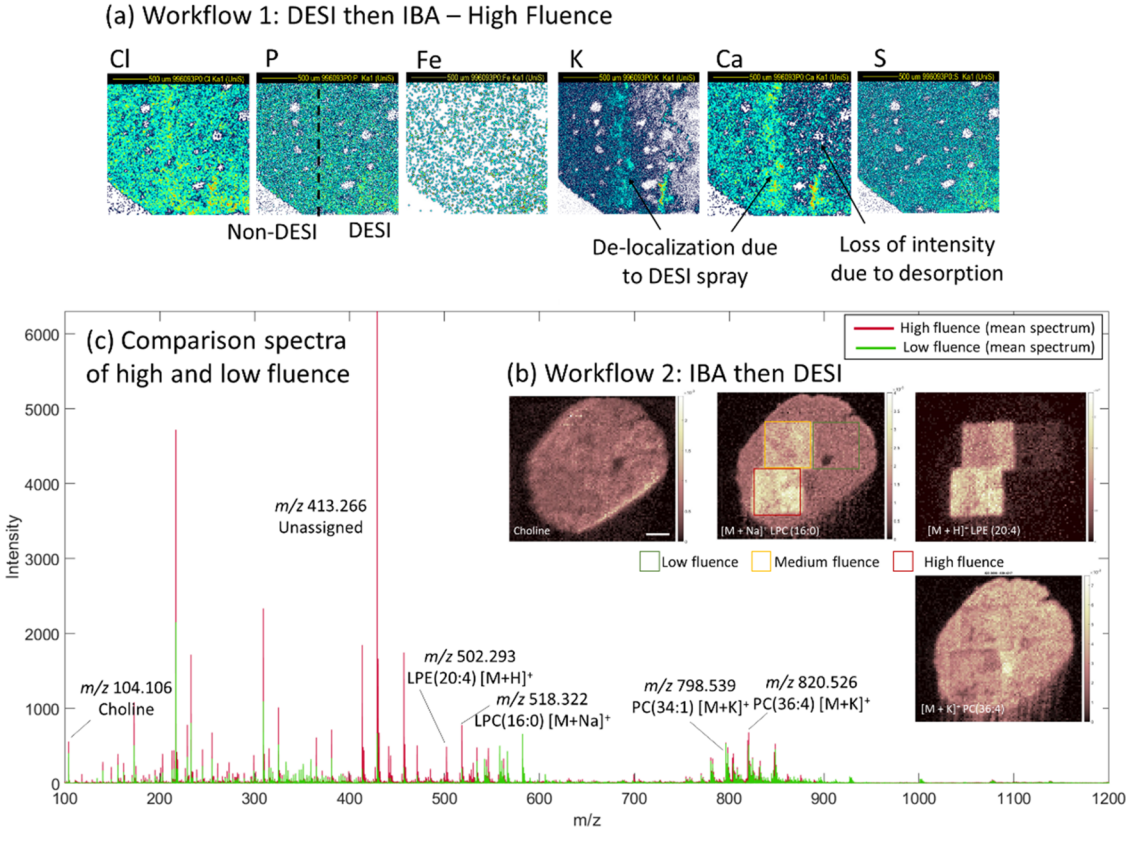


**Figure 2.** Sequential DESI-PIXE and PIXE-DESI analysis: (a) PIXE maps (Workflow 1; DESI then PIXE), where right half of field of view was previously imaged using DESI, showing Cl, P, Fe, K, Ca, and S; (b) DESI images (normalized to total ion intensity) of $m/z$ 104.106 (choline); $m/z$ 518.302 ($[M + Na]^+$ LPC(16:0)); $m/z$ 502.293 ($[M + H]^+$ LPE(20:4)); and $m/z$ 820.525 ($[M + K]^+$ PC(36:4)), corresponding to "Workflow 2" (PIXE then DESI), and showing lipid changes upon irradiation; and (c) overlay of mass spectra, from ROIs of high (red) and low (green) fluence.

As well as minor elements, the trace elements Cu, Fe, Zn, and Cr were detected in the tissue on PET but were not detected in the tissues on Si, carbon foil, and HOPG, due to increased Bremsstrahlung background and/or substrate



https://doi.org/10.1021/acs.analchem.1c01927
Anal. Chem. 2021, 93, 13450−13458

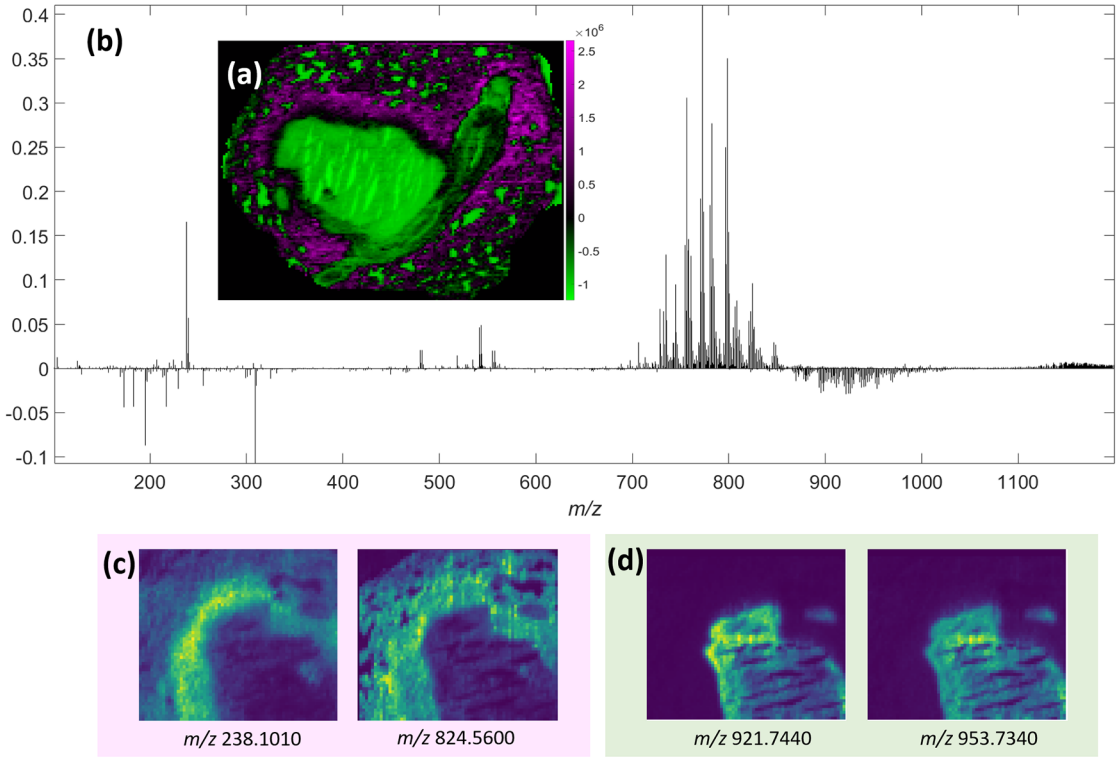


**Figure 3.** Principal component analysis of tissue imaged with DESI (and subsequently imaged using PIXE), where (a) shows principal component (PC) 1 image and (b) shows the corresponding loadings spectrum. The green pixels correspond to negative eigenvectors, while positive eigenvectors are pink. Panels (c) and (d) are selected ion images from positive and negative eigenvectors, respectively. Supporting Information Table S4 lists the Top 20 scores and loadings, along with tentative assignments and ppm errors.

impurities. Therefore, PET was determined to be the most compatible of the substrates for PIXE imaging. An additional advantage of the PET substrate is the compatibility with staining techniques and laser capture microdissection.[53]

*MALDI.* The PET was not compatible with MALDI, as the laser caused holes to form on the substrate. Mass spectrometry images could be obtained using HOPG or carbon foil substrates but were inferior to images produced on standard glass substrates (Supporting Information Figure S4).

*DESI.* The same substrates were investigated for compatibility with DESI. Here, the PET yielded the highest contrast images compared with the other substrates, as shown in Figure 1. It is worthy of note that it was necessary to place a glass slide behind the PET membrane to give enough mechanical rigidity to generate clear DESI images. In this arrangement, the PET actually outperformed the standard glass substrate typically used for DESI imaging, by providing higher contrast images.

The MALDI and DESI data sets were interrogated for $m/z$ values corresponding to 30 candidate biomolecules (comprising a selection of intact lipids, lipid metabolites, and small molecules). Ion images were produced to determine whether the tissue could be visualized on the substrates tested, and the outcome is presented in Supporting Information Table S3. The data show that, as well as providing high contrast images, the use of a PET substrate for DESI imaging gives comparable coverage to glass over a range of candidate biomolecules.

**Investigating Workflows.** None of the substrates tested here were fully compatible with sequential IBA and MALDI imaging. However, PET showed good compatibility with both DESI and PIXE, giving an opportunity to explore sequential IBA and MSI analyses on the same sample.

The proceeding set of investigations explored the appropriate workflow to maximize the information available from sequential elemental and molecular imaging. Two workflows were investigated (Supporting Information Figure S5). In "Workflow 1," DESI was carried out prior to IBA, to determine whether the DESI delocalizes minor and/or trace elements. In "Workflow 2," IBA was carried at three different fluences (with increasing fluence corresponding to greater acquisition time and sensitivity to trace elements) on three different 2 mm × 2 mm locations on the tissue. The whole tissue was then imaged with DESI to determine the effect of prior ion beam analysis on selected biomolecules present in the tissue homogenate.

*DESI Followed by IBA—Workflow 1.* Figure 2a shows PIXE maps for tissue homogenates mounted on PET for Workflow 1, where only half of the area had been previously imaged with DESI, as indicated on the image. The PIXE maps for Ca and K show a tidemark at the edge of the DESI analysis area, indicating delocalization. This is consistent with previous observations that alkali metals delocalize after formalin-fixed paraffin-embedded (FFPE) preparation of tissue because these elements are usually unbound to molecular structures in tissues and so are mobile.[54] The PIXE maps for S, P, and Fe show no displacement due to the DESI analysis. This indicates that this workflow could be used if Group I and II metals are not of interest.

*IBA Followed by DESI—Workflow 2.* Figure 2(b, inset) shows extracted ion images for Workflow 2 (IBA then DESI) for ions assigned to choline, LPC(16:0), LPE(20:4), and PC(36:4). The locations of the 2 mm × 2 mm areas previously analyzed by PIXE at low, medium, and high fluence are highlighted by yellow, green, and red squares, respectively. It is


https://doi.org/10.1021/acs.analchem.1c01927
Anal. Chem. 2021, 93, 13450−13458

clear from Figure 2b that prior PIXE analysis at low fluence has a very little observable impact on lipids. Supporting Information Figure S1 shows example PIXE images that are produced at this low fluence. The images are sufficient to localize S, K, Cl, and S in the tissue, but the sensitivity is not sufficient to image the distribution of Fe.

At higher fluences, the images in Figure 2b show that the intensity of the lower mass lipids, LPC(16:0) and LPE(20:4), increases. In contrast, there is a slight reduction in signal for PC(36:4) in irradiated regions. This behavior (namely loss of intensity of intact lipids and increased intensity of lipid metabolites upon irradiation) can be explained by ion beam-induced fragmentation.

In Figure 2c, the mass spectra from ROIs corresponding to areas of low fluence—(green) and high fluence irradiation (red) are overlaid. The spectra show that irradiation produces new peaks in the $m/z$ 400−500 range, but also that peaks around $m/z$ 750−900 are relatively unaffected by prior ion beam irradiation, see Supporting Information Figure S6. Figure 2b shows that this is also the case for choline.

**Application to a Real Tissue Sample.** Here, we demonstrate the suitability of Workflow 1 (DESI followed by PIXE) for a practical application. Fresh frozen rabbit lung tissue containing a caseous granuloma (a lesion caused by tuberculosis) was used as a demonstration sample. Optical images are presented in Supporting Information Figure S7. Four sequential tissue sections were mounted on the PET slide and labeled A to D (from left to right). Section C was imaged using DESI, under a standard imaging protocol for small molecules. As shown in Figure 3, the method was sufficient to image many lipid species in the different compartments of the granuloma sample, showing spatial organization of lipids in granuloma tissue, as reported in the previous work.[55]

Section C (post-DESI) and the neighboring Section B (control) were then imaged using PIXE. The images for Fe, Zn, and S, as well as the spectra are compared in Figure 4. The remaining elemental images are presented in Supporting Information Figure S8. The intensities of K and Cl are lower in the sample previously imaged using DESI compared to the control sample. However, as observed in the homogenized tissue, the S and Fe distribution are unaffected by prior DESI analysis.

Figure 5a shows overlays of S (from PIXE) and TAG (58:8) (from DESI) from the same tissue sample. These analytes are used for image registration, as they both clearly denote the caseum (necrotic) region of the granuloma sample. Figure 5b,c shows that the Fe detected by PIXE overlays well with $m/z$ 832 (assigned to PC(38:4)) and $m/z$ 544.3 (assigned to LPC(18:1)) detected by DESI, shown previously to be important markers in TB pathogenesis.[55]

## DISCUSSION

These results show that it is possible to locate elemental and molecular markers on the same tissue section with IBA and DESI at the 50 $\mu$m scale. Some changes are observed, depending on which analysis is carried out first.

If Group I and II metals are not of interest, we propose that molecular imaging using DESI is carried out prior to elemental imaging using IBA. DESI followed by IBA imposed no compromise on the quality of mass spectrometry images. This work has shown that Fe, S, and Zn do not delocalize during DESI analysis. This finding is significant because it also shows the applicability of imaging these elements with other methods

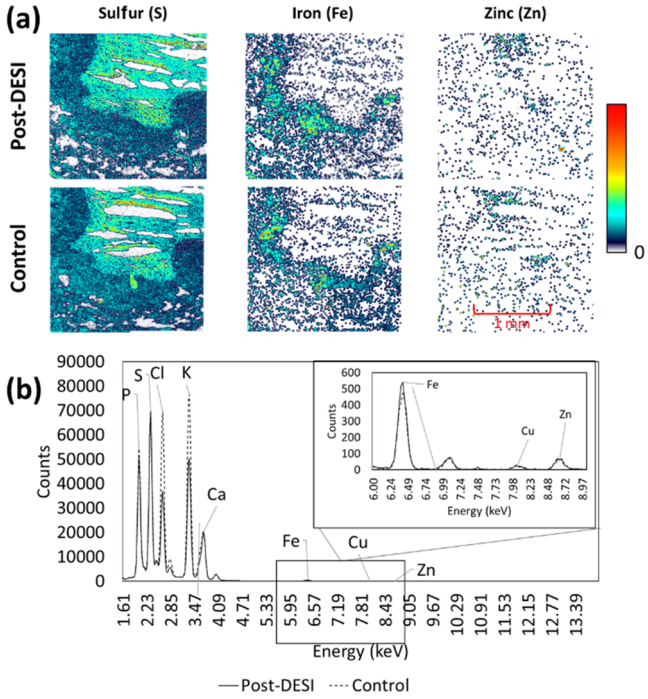


**Figure 4.** (a) Sulfur (S), iron (Fe), and zinc (Zn) elemental maps obtained using PIXE after DESI (top row) and on a control sample (no prior measurements; bottom row) and (b) overlay of X-ray spectra from post-DESI and the control sample.

(e.g., XRF or LA-ICP-MS) following DESI. However, delocalization of Group I or II metals was found to occur when DESI was performed first. Therefore, if mobile ions (such as Cl, Ca, and K) are of most interest, then IBA should be carried out first. If the fluence of the IBA measurement is kept low, minimal beam damage is observed. However, restricting the IBA measurement fluence comes at a cost of lower sensitivity to trace elements. To increase sensitivity, the PIXE measurement time can be extended (higher fluence), but this comes at the expense of changes to the molecular compounds, such as fragmentation of lipids or enhancement of lipid metabolites.

This work has shown that not all lipids respond to ion beam irradiation in the same way—while lipid signals in the $m/z$ 400−500 range were augmented by prior ion beam imaging, the impact on lipids at $m/z$ 750−900 was less pronounced. It is known that lipid stability is influenced by various factors including oxidation and heat[56] as well as lipid class.[57] This explains the differential behavior of different $m/z$ peaks upon proton beam irradiation. Future work should explore how proton beam damage to lipids can be mitigated, for example, using a cold sample stage, measurement at ambient pressure, or different scan patterns and scan rates.

It should be noted that a compatible substrate for sequential MALDI and IBA imaging was not found in this work. In X-ray microanalysis, one approach has been to suspend tissues over a metal frame,[29] but thin tissue sections are often not mechanically self-supporting. An alternative approach has been the use of 50 nm silicon nitride windows, but the cost, small area, and brittle nature of this material make it difficult to work with. Future work should seek alternative candidate substrates that are low Z, with few elemental impurities, and resistant to the MALDI laser energy.


https://doi.org/10.1021/acs.analchem.1c01927
Anal. Chem. 2021, 93, 13450−13458

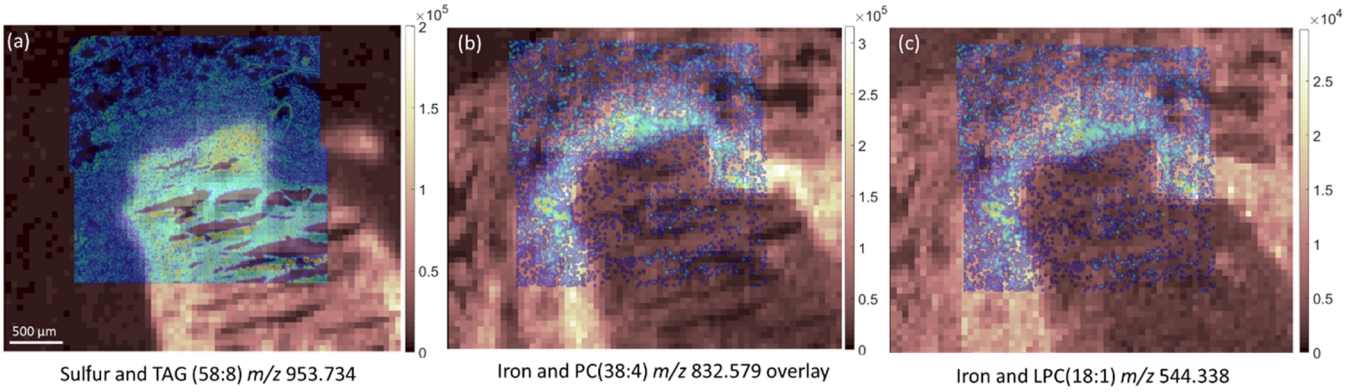


**Figure 5.** Overlay of the same tissue section sequentially analyzed using PIXE (blue) and DESI (brown) of (a) S and $[M + Na]^+$ TAG(58:8) $m/z$ 953.7430, (b) Fe and $[M + K]^+$ PC(38:4) $m/z$ 832.579, and (c) Fe and $[M + Na]^+$ LPC(18:0) $m/z$ 544.338.

## CONCLUSIONS

We have demonstrated a method for correlating the trace elements, Fe, S, and Zn with lipid profiles in fresh frozen tissue samples, at 50 $\mu$m resolution. The colocation of Fe and lipids in tissues is novel. Since iron overload can result in oxidative stress and subsequent damage to lipid membranes,[58] methods to colocate Fe with lipid profiles will help study these processes in a range of acute and chronic inflammatory conditions, such as Parkinson's disease, cancer, and tuberculosis.

## ASSOCIATED CONTENT

### Supporting Information

The Supporting Information is available free of charge at https://pubs.acs.org/doi/10.1021/acs.analchem.1c01927.

Additional PIXE, DESI, and MALDI data including elemental and molecular maps, tabulated data on investigated substrates and optical images (PDF)

## AUTHOR INFORMATION


### Corresponding Author

**Melanie J. Bailey** − *Department of Chemistry, University of Surrey, Guildford GU2 7XH, U.K.;* orcid.org/0000-0001-9050-7910; Email: m.bailey@surrey.ac.uk

### Authors

**Janella Marie de Jesus** − *Department of Chemistry, University of Surrey, Guildford GU2 7XH, U.K.*

**Catia Costa** − *University of Surrey Ion Beam Centre, University of Surrey, Guildford GU2 7XH, U.K.*

**Amy Burton** − *The National Physical Laboratory, Teddington, Middlesex TW11 0LW, U.K.*

**Vladimir Palitsin** − *University of Surrey Ion Beam Centre, University of Surrey, Guildford GU2 7XH, U.K.*

**Roger Webb** − *University of Surrey Ion Beam Centre, University of Surrey, Guildford GU2 7XH, U.K.*

**Adam Taylor** − *The National Physical Laboratory, Teddington, Middlesex TW11 0LW, U.K.;* orcid.org/0000-0003-0501-8886

**Chelsea Nikula** − *The National Physical Laboratory, Teddington, Middlesex TW11 0LW, U.K.;* orcid.org/0000-0002-6817-2592

**Alex Dexter** − *The National Physical Laboratory, Teddington, Middlesex TW11 0LW, U.K.;* orcid.org/0000-0001-8536-4417

**Firat Kaya** − *Department of Microbiology and Molecular Genetics, New Jersey Medical School, Rutgers, The State University of New Jersey, Newark 07102, United States*

**Mark Chambers** − *Department of Microbial Sciences, Faculty of Health and Medical Sciences, University of Surrey, Guildford, Surrey GU2 7XH, U.K.*

**Veronique Dartois** − *Center for Discovery and Innovation, Hackensack School of Medicine, Nutley, New Jersey 07110, United States; Department of Microbiology and Molecular Genetics, New Jersey Medical School, Rutgers, The State University of New Jersey, Newark 07102, United States;* orcid.org/0000-0001-9470-5009

**Richard J. A. Goodwin** − *Imaging and Data Analytics, Clinical Pharmacology and Safety Science, Cambridge CB2 0AA, U.K.; Institute of Infection, Immunity and Inflammation, College of Medical, Veterinary and Life Sciences, University of Glasgow, Glasgow G12 8TA, U.K.*

**Josephine Bunch** − *The National Physical Laboratory, Teddington, Middlesex TW11 0LW, U.K.*

Complete contact information is available at: https://pubs.acs.org/10.1021/acs.analchem.1c01927


### Notes

The authors declare no competing financial interest.

## ACKNOWLEDGMENTS

This study was funded by an EPSRC strategic equipment award (EP/P001440/1) and an EPSRC sponsored fellowship (EP/R031118/1), the Surrey-NPL studentship fund. Beam time was provided by EPSRC National Research Facility UKNIBC NS/A000059/1 and RADIATE (Horizon 2020, grant agreement No 824096, proposal 19001813-ST). Special thanks to John Swales from AstraZeneca for providing tissue homogenates. The authors acknowledge R.T. Steven from NPL for experimental support. The authors thank Laura E Via and Danielle Weiner from the NIAID-NIH for providing infected lung tissues.

## REFERENCES

(1) Szpunar, J. *Analyst* **2005**, *130*, 442−465.

(2) Naga Raju, G. J.; John Charles, M.; Bhuloka Reddy, S.; Sarita, P.; Seetharami Reddy, B.; Rama Lakshmi, P. V. B.; Vijayan, V. *Nucl. Instrum. Methods Phys. Res., Sect. B* **2005**, *229*, 457−464.

(3) Rajendran, R.; Minqin, R.; Ronald, J. A.; Rutt, B. K.; Halliwell, B.; Watt, F. *Free Radical Biol. Med.* **2012**, *53*, 1675−1679.

(4) Ren, M. Q.; Ji, X.; Vajandar, S. K.; Mi, Z. H.; Hoi, A.; Walczyk, T.; Van Kan, J. A.; Bettiol, A. A.; Watt, F.; Osipowicz, T. *Nucl. Inst. Methods Phys. Res., Sect. B* **2017**, *406*, 15−24.
(5) Jeynes, J. C. G.; Bailey, M. J.; Coley, H.; Kirkby, K. J.; Jeynes, C. *Nucl. Instrum. Methods Phys. Res., Sect. B* **2010**, *268*, 2168−2171.
(6) Ceko, M. J.; Hummitzsch, K.; Hatzirodos, N.; Rodgers, R. J.; Harris, H. H. *Metallomics* **2015**, *7*, 828−836.
(7) Ceko, M. J.; Hummitzsch, K.; Hatzirodos, N.; Bonner, W.; James, S. A.; Kirby, J. K.; Rodgers, R. J.; Harris, H. H. *Metallomics* **2015**, *7*, 756−765.
(8) Collingwood, J. F.; Adams, F. *Spectrochim. Acta, Part B* **2017**, *130*, 101−118.
(9) Farquharson, M. J.; Geraki, K.; Falkenberg, G.; Leek, R.; Harris, A. *Appl. Radiat. Isot.* **2007**, *65*, 183−188.
(10) Rajendran, R.; Minqin, R.; Ronald, J. A.; Rutt, B. K.; Halliwell, B.; Watt, F. *Free Radical Biol. Med.* **2012**, *53*, 1675−1679.
(11) Kaabar, W.; Daar, E.; Bunk, O.; Farquharson, M. J.; Laklouk, A.; Bailey, M.; Jeynes, C.; Gundogdu, O.; Bradley, D. A. *Nucl. Instrum. Methods Phys. Res., Sect. A* **2011**, *652*, 786−790.
(12) Ugarte, M.; Grime, G. W.; Lord, G.; Geraki, K.; Collingwood, J. F.; Finnegan, M. E.; Farnfield, H.; Merchant, M.; Bailey, M. J.; Ward, N. I.; Foster, P. J.; Bishop, P. N.; Osborne, N. N. *Metallomics* **2012**, *4*, 1245−1254.
(13) Vavpetič, P.; Pelicon, P.; Vogel-Mikuš, K.; Grlj, N.; Pongrac, P.; Jeromel, L.; Ogrinc, N.; Regvar, M. *Nucl. Instrum. Methods Phys. Res., Sect. B* **2013**, *306*, 140−143.
(14) Carmona, A.; Devès, G.; Ortega, R. *Anal. Bioanal. Chem.* **2008**, *390*, 1585−1594.
(15) Carboni, E.; Nicolas, J.-D.; Töpperwien, M.; Stadelmann-Nessler, C.; Lingor, P.; Salditt, T. *Biomed. Opt. Express* **2017**, *8*, 4331−4347.
(16) Devès, G.; Isaure, M. P.; Le Lay, P.; Bourguignon, J.; Ortega, R. *Nucl. Instrum. Methods Phys. Res., Sect. B* **2005**, *231*, 117−122.
(17) Eberlin, L. S.; Liu, X.; Ferreira, C. R.; Santagata, S.; Agar, N. Y. R.; Cooks, R. G. *Anal. Chem.* **2011**, *83*, 8366−8371.
(18) Matusch, A.; Fenn, L. S.; Depboylu, C.; Klietz, M.; Strohmer, S.; McLean, J. A.; Becker, J. S. *Anal. Chem.* **2012**, *84*, 3170−3178.
(19) Svirkova, A.; Turyanskaya, A.; Perneczky, L.; Streli, C.; Marchetti-Deschmann, M. *Analyst* **2018**, *143*, 2587−2595.
(20) Touboul, D.; Roy, S.; Germain, D. P.; Chaminade, P.; Brunelle, A.; Laprévote, O. *Int. J. Mass Spectrom.* **2007**, *260*, 158−165.
(21) Flint, L. E.; Hamm, G.; Ready, J. D.; Ling, S.; Duckett, C. J.; Cross, N. A.; Cole, L. M.; Smith, D. P.; Goodwin, R. J. A.; Clench, M. R. *Anal. Chem.* **2020**, *92*, 12538−12547.
(22) Colliver, T. L.; Brummel, C. L.; Pacholski, M. L.; Swanek, F. D.; Ewing, A. G.; Winograd, N. *Anal. Chem* **1997**, *69*, 2225−2231.
(23) Hill, M. W.; Mangelson, N. F.; Ryder, J. F.; Atwood, N. D.; Wood, B. W. Trace Element Analysis of Wild Rodent Tissues Using the PIXE Method. In *International Conference on Nuclear Methods in Environment and Energy Research*; Columbia, 1980, pp 549−559.
(24) Lindh, U.; Brune, D.; Nordberg, G.; Wester, P. O. *Sci. Total Environ.* **1980**, *16*, 109−116.
(25) Maenhaut, W.; De Reu, L.; Van Rinsvelt, H. A.; Cafmeyer, J.; Van Espen, P. *Nucl. Instrum. Methods* **1980**, *168*, 557−562.
(26) Bradley, D. A.; Farquharson, M. J.; Gundogdu, O.; Al-Ebraheem, A.; Che Ismail, E.; Kaabar, W.; Bunk, O.; Pfeiffer, F.; Falkenberg, G.; Bailey, M. *Radiat. Phys. Chem.* **2010**, *79*, 162−175.
(27) Ugarte, M.; Grime, G. W.; Lord, G.; Geraki, K.; Collingwood, J. F.; Finnegan, M. E.; Farnfield, H.; Merchant, M.; Bailey, M. J.; Ward, N. I.; Foster, P. J.; Bishop, P. N.; Osborne, N. N. *Metallomics* **2012**, *4*, 1245−1254.
(28) Garman, E. F.; Grime, G. W. *Prog. Biophys. Mol. Biol.* **2005**, *89*, 173−205.
(29) Punzón-Quijorna, E.; Kelemen, M.; Vavpetič, P.; Kavalar, R.; Pelicon, P.; Fokter, S. K. *Nucl. Instrum. Methods Phys. Res., Sect. B* **2020**, *462*, 182−186.
(30) Landsberg, J. P.; McDonald, B.; Watt, F. *Nature* **1992**, *360*, 65−68.
(31) Verma, H. R. X-Ray Fluoresence (XRF) and Particle Induced X-Ray Emission (PIXE). In *Atomic and Nuclear Analytical Methods*; Springer: Berlin, Heidelberg, 2007; Vol. *92*, pp 1−73.
(32) Natasi, M.; Mayer; James, W.; Wang, Y. Particle Induced X-Ray Emission (PIXE). In *Ion Beam Analysis: Fundamentals and Applications*; CRC Press, 2014; pp 141−1551.
(33) Jeynes, C.; Bailey, M. J.; Bright, N. J.; Christopher, M. E.; Grime, G. W.; Jones, B. N.; Palitsin, V. V.; Webb, R. P. *Nucl. Instrum. Methods Phys. Res., Sect. B* **2012**, *271*, 107−118.
(34) Miliszkiewicz, N.; Walas, S.; Tobiasz, A. *J. Anal. At. Spectrom.* **2015**, *30*, 327−338.
(35) Nakata, Y.; Honda, Y.; Ninomiya, S.; Seki, T.; Aoki, T.; Matsuo, J. *Appl. Surf. Sci.* **2008**, *255*, 1591−1594.
(36) Wakamatsu, Y.; Yamada, H.; Ninomiya, S.; Jones, B. N.; Seki, T.; Aoki, T.; Webb, R.; Matsuo, J. *Nuclear Instrum. Methods Physics Res., Sect. B* **2011**, *269*, 2251−2253.
(37) Jenčič, B.; Vavpetič, P.; Kelemen, M.; Vencelj, M.; Vogel-Mikuš, K.; Kavčič, A.; Pelicon, P. *J. Am. Soc. Mass Spectrom.* **2019**, *30*, 1801−1812.
(38) Jeromel, L.; Siketić, Z.; Potočnik, N. O.; Vavpetič, P.; Rupnik, Z.; Bučar, K.; Pelicon, P. *Nucl. Inst. Methods Phys. Res., Sect. B* **2014**, *332*, 22−27.
(39) Laskin, J.; Heath, B. S.; Roach, P. J.; Cazares, L.; Semmes, O. J. *Anal. Chem.* **2012**, *84*, 141−148.
(40) Kompauer, M.; Heiles, S.; Spengler, B. *Nat. Methods* **2017**, *14*, 90−96.
(41) Swales, J. G.; Strittmatter, N.; Tucker, J. W.; Clench, M. R.; Webborn, P. J. H.; Goodwin, R. J. A. *Sci. Rep.* **2016**, *6*, No. 37648.
(42) Subbian, S.; Tsenova, L.; Yang, G.; O'Brien, P.; Parsons, S.; Peixoto, B.; Taylor, L.; Fallows, D.; Kaplan, G. *Open Biol.* **2011**, *1*, No. 110016.
(43) Blanc, L.; Sarathy, J. P.; Cabrera, N. A.; O'Brien, P.; Dias-Freedman, I.; Mina, M.; Sacchettini, J.; Savic, R. M.; Gengenbacher, M.; Podell, B. K.; Prideaux, B.; Ioerger, T.; Dick, T.; Dartois, V. *J. Exp. Med.* **2018**, *215*, 1975−1986.
(44) Zimmerman, M.; Blanc, L.; Chen, P. Y.; Dartois, V.; Prideaux, B. *J. Visusalized Exp.* **2018**, *134*, No. e57402.
(45) Gomez-Morilla, I.; Simon, A.; Simon, R.; Williams, C. T.; Kiss, ÁZ.; Grime, G. W. *Nucl. Instrum. Methods Phys. Res., Sect. B* **2006**, *249*, 897−902.
(46) Chambers, M. C.; et al. *Nat. Biotechnol.* **2012**, *30*, 918−920.
(47) Race, A. M.; Styles, I. B.; Bunch, J. *J. Proteomics* **2012**, *75*, 5111−5112.
(48) Race, A. M.; Palmer, A. D.; Dexter, A.; Steven, R. T.; Styles, I. B.; Bunch, J. *Anal. Chem.* **2016**, *88*, 9451−9458.
(49) Šmit, Ž.; Pelicon, P.; Vidmar, G.; Zorko, B.; Budnar, M.; Demortier, G.; Gratuze, B.; Šturm, S.; Nečemer, M.; Kump, P.; Kos, M. *Nucl. Instrum. Methods Phys. Res., Sect. B* **2000**, *161−163*, 718−723.
(50) Vavpetič, P.; Pelicon, P.; Vogel-Mikuš, K.; Grlj, N.; Pongrac, P.; Jeromel, L.; Ogrinc, N.; Regvar, M. *Nucl. Instrum. Methods Phys. Res., Sect. B* **2013**, *306*, 140−143.
(51) Wang, Y. D.; Mesjasz-Przybylowicz, J.; Tylko, G.; Barnabas, A. D.; Przybylowicz, W. J. *Nucl. Instrum. Methods Phys. Res., Sect. B* **2013**, *306*, 134−139.
(52) van der Ent, A.; Przybyłowicz, W. J.; de Jonge, M. D.; Harris, H. H.; Ryan, C. G.; Tylko, G.; Paterson, D. J.; Barnabas, A. D.; Kopittke, P. M.; Mesjasz-Przybyłowicz, J. *New Phytol.* **2018**, *218*, 432−452.
(53) Morrogh, M.; Olvera, N.; Bogomolniy, F.; Borgen, P. I.; King, T. A. *Biotechniques* **2007**, *43*, 41−48.
(54) Bonta, M.; Török, S.; Hegedus, B.; Döme, B.; Limbeck, A. *Anal. Bioanal. Chem.* **2017**, *409*, 1805−1814.
(55) Marakalala, M. J.; Raju, R. M.; Sharma, K.; Zhang, Y. J.; Eugenin, E. A.; Prideaux, B.; Daudelin, I. B.; Chen, P. Y.; Booty, M. G.; Kim, J. H.; Eum, S. Y.; Via, L. E.; Behar, S. M.; Barry, C. E.; Mann, M.; Dartois, V.; Rubin, E. J. *Nat. Med.* **2016**, *22*, 531−538.
(56) Ulmer, C. Z.; Koelmel, J. P.; Jones, C. M.; Garrett, T. J.; Aristizabal-Henao, J. J.; Vesper, H. W.; Bowden, J. A. *Lipids* **2021**, *56*, 3−16.


https://doi.org/10.1021/acs.analchem.1c01927
*Anal. Chem.* 2021, 93, 13450−13458

(57) Shahidio, F.; Ying, Z. *Chem. Soc. Rev.* **2010**, *39*, 4067−4079.
(58) Gonzalez, P.; Piloni, N.; Puntarulo, S. Iron Overload and Lipid Peroxidation in Biological Systems. In *Lipid Peroxidation*; InTech, 2012; pp 89−90.



https://doi.org/10.1021/acs.analchem.1c01927
*Anal. Chem.* 2021, 93, 13450−13458